



**HAL**  
open science

## Confidence map tool for gradient based X-ray phase contrast imaging

Adrien Stolidi, Georges Giakoumakis, Jérôme Primot, Amélie Jarnac, David Tisseur

► **To cite this version:**

Adrien Stolidi, Georges Giakoumakis, Jérôme Primot, Amélie Jarnac, David Tisseur. Confidence map tool for gradient based X-ray phase contrast imaging. *Optics Express*, 2022, 30 (3), pp.4302-4311. 10.1364/OE.438876 . cea-04001315

**HAL Id: cea-04001315**

**<https://cea.hal.science/cea-04001315>**

Submitted on 22 Feb 2023

**HAL** is a multi-disciplinary open access archive for the deposit and dissemination of scientific research documents, whether they are published or not. The documents may come from teaching and research institutions in France or abroad, or from public or private research centers.

L'archive ouverte pluridisciplinaire **HAL**, est destinée au dépôt et à la diffusion de documents scientifiques de niveau recherche, publiés ou non, émanant des établissements d'enseignement et de recherche français ou étrangers, des laboratoires publics ou privés.

# Confidence Map tool for gradient-based X-ray phase contrast imaging

ADRIEN STOLIDI,<sup>1\*</sup> GEORGES GIAKOUMAKIS,<sup>1,2</sup> JÉRÔME PRIMOT,<sup>2</sup>  
AND DAVID TISSEUR<sup>1</sup>

<sup>1</sup>Université Paris-Saclay, CEA, List, F-91120, Palaiseau, France

<sup>2</sup>Université Paris-Saclay, ONERA, DOTA, F-91123 Palaiseau, France

\*adrien.stolidi@cea.fr

**Abstract:** We present a graphical tool that we call a "confidence map". It allows to evaluate locally the quality of a phase image extracted from the measurement of its gradients. The tool is primarily used to alert the observer to the presence of artifacts that could affect his interpretation of the image. It can also be used to optimize a phase imager since it associates a cause with the creation of each artifact: noise, aliasing and dislocation. An illustration of the use of this confidence map tool is presented based on a microfocus X-ray tube using multilateral shearing interferometry, a gradient based phase contrast technique employing a single 2D-grating.

© 2021 Optical Society of America under the terms of the [OSA Open Access Publishing Agreement](#)

## 1. Introduction

X-ray phase imaging is of great interest for improving the contrast of low-density material, in complementarity with classical absorption imaging. If different techniques can be found in the literature [1], we propose to consider here those which consist in inserting a phase modulator in the optical path which will produce a reference intensity pattern at the detector. Variation of this pattern induced by a sample will allow a measurement of the phase gradient signal. One type of intensity modulator produces an intensity pattern randomly distributed in the detector plane, such as the ones used for the speckle-based techniques [2–4] and other uses regular intensity pattern like 1D or 2D grating based interferometry techniques [5–12].

All these techniques are able to measure a minimum of two orthogonal gradients in one or multiple acquisitions. With these, an interesting way to evaluate the quality of the differential phase measurement (and also of the phase image extracted) is to calculate a phase derivative closure map  $C(x, y)$ , defined for the first time by Jennison [13] and applied in the X-ray domain on synchrotron light source by Rizzi *et al.* [14]. Assuming that the wavefront issued from the sample can be viewed as a continuous surface, derivable twice for each point on this surface, the circulation around it should be equal to zero. In other words, if we consider two orthogonal phase gradients  $[\partial_x \phi(x, y), \partial_y \phi(x, y)]$  and apply a curl operator, the phase derivative closure map should be equal to zero:

$$C(x, y) = \partial_x [\partial_y \phi(x, y)] - \partial_y [\partial_x \phi(x, y)] = 0 \quad (1)$$

But in real conditions, different contributions of  $C(x, y)$  can arise, and Eq.1 can be rewritten as

$$C(x, y) = \epsilon_a + \epsilon_n + \epsilon_d \quad (2)$$

where  $\epsilon_a$  reveals an aliasing problem. This means that the phase variation to be measured evolves too fast spatially compared to the sampling step of the intensity patterns (fringes or speckles).  $\epsilon_d$  reveals that the phase signal is dislocated [15] due to a local extinction of the intensity, and  $\epsilon_n$  reveals the noise on the phase gradient measured. This phase derivative closure map can be calculated for every type of gradient-based X-ray phase contrast technique. We propose to use  $C(x, y)$  in order to build a confidence map which can be used as an indicator

of the phase retrieval image quality. The following section will introduce how to build the confidence map by estimating the parameters  $\epsilon_a$ ,  $\epsilon_d$  and  $\epsilon_n$  from Eq. (2) using simulation images. Then, an experimental application on a canonical object will be presented.

## 2. How to build a confidence map

To illustrate the estimation of the parameters  $\epsilon_a$ ,  $\epsilon_d$  and  $\epsilon_n$  and build a confidence map, we propose to use a phase contrast simulation tool based on wave-front description of the multilateral shearing interferometry technique [16]. The diffracted orders are directly simulated after the 2D-checkerboard grating and propagate onto the detection plan. A simple object with analytical description can be imported into the simulated scene. Two configurations are possible depending on whether the sample is placed before or after the modulator. We have chosen here the second implementation, but this has no major effect on the principle of the confidence map. Here, we are going to consider an ideal case with monochromatic source at 17.48 keV (molybdenum  $K\alpha$  line) and a detection plane with pixel size  $S_{pix}$  of  $6 \times 6 \mu\text{m}^2$ . The object simulated is a PMMA cylinder of 500  $\mu\text{m}$  of diameter. The simulated grating, placed at 4 cm from the object, has an orthogonal periodicity  $a$  of  $a = 12 \mu\text{m}$  with a  $0-\pi$  shift at Mo  $K\alpha$ . The total distance is 60 cm and the source-grating distance is 14 cm leading to a magnification  $G = 4.3$ . The sample magnification is  $G = 6$ . To complete the simulation a Gaussian noise is added, since it is a fair description of the experimental noise measured in our setup. From this, a simulated phase gradient is evaluated and a phase derivative closure map  $C(x, y)$  is calculated [14] (see respectively Figure 1 left and right image). With these two images, the plot profiles are presented on Figure 1 (bottom left).

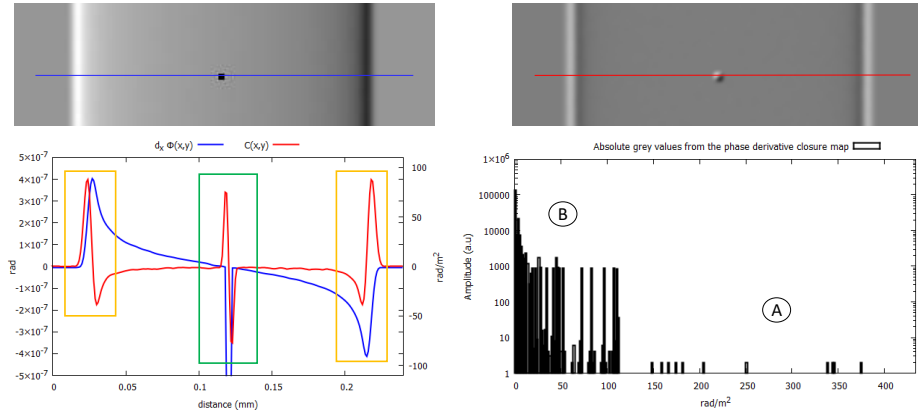


Fig. 1. Simulation of PMMA cylinder with the inclusion of a defect in the center, for a monochromatic X-ray source at 17.48 keV. Top-left, phase gradient with local extinction. Top-right, phase derivative closure map. Bottom-left, corresponding plot profile. Bottom-right, histogram of the phase derivative closure map (absolute values).

First, the blue plot shows a slow phase variation in radian per meter with a more abrupt variation at the edges of the cylinder (see orange rectangles). This is due to a weak fringes sampling in this local area of the cylinder, leading to a non-accurate phase gradient measurement. This area is emphasized by the phase derivative closure map, plotted in red, in radian per square meter. We can see that when an unsuspected strong phase variation arises,  $C(x, y)$  value underlines this phenomenon (orange rectangles) and even more so when a local phase extinction occurs (see green rectangle). Indeed, in this case the  $C(x, y)$  value has an even greater peak-to-peak value. Finally, the histogram of the absolute gray values of the phase derivative closure map shows two areas. The first one (see label A) with few counts and high values of  $C(x, y)$  (tens of hundreds

of  $\text{rad/m}^2$ ) highlighting the first parameter estimate: the phase dislocation  $\epsilon_d$ . Indeed, phase dislocation are very intense and local, therefore  $C(x, y)$  values correlated with this phenomenon are few, precisely located and correspond to high intensity values. To extract these values, threshold methods can be applied. For instance, here a threshold  $T_{hd}$  is defined, based on maximum entropy method [17]. It consists of measuring the uncertainty of an event taking place, in this case a phase dislocation. A derivative method, such as the Shanbhag method [18], can be also evaluated on  $C(x, y)$ . After the definition of the threshold, an evaluation pixel-to-pixel of the  $C(x, y)$  image is made, and an alert is generated by coloring the pixel in red when the pixel value  $(x_i, y_j) > T_{hd}$ .

The second area of the histogram, (see label B Figure 1) has more counts, but with smaller  $C(x, y)$  intensity values (a few dozen of  $\text{rad/m}^2$ ). This is related to the aliasing  $\epsilon_a$  phenomenon. The high counts reveal that a significant portion of the image is impacted by  $\epsilon_a$ . Notice that the aliasing being more important in the area of the object with strong variations, for instance here, at the edge of the cylinder. An average evaluation of the phase derivative can be made without values correlated to  $\epsilon_d$ . A square region of interest  $\Omega$  of size of  $S_\Omega = aG/(2S_{pix})$  with the following odd condition  $\{2S_\Omega + 1 \mid S_\Omega \in \mathbb{N}\}$  is defined.  $S_\Omega$  corresponds to the phase sensitivity measurement reachable by using a fringe interference pattern of periodicity  $aG$ , sampling by the detection plan of pixel size  $S_{pix}$ . Evaluation of  $C(x_i, y_j)$  in  $\Omega$  leads to an average value related to noise  $\epsilon_n$  and aliasing  $\epsilon_a$ . In order to distinguish the contribution of  $\epsilon_n$  from  $\epsilon_a$  a binarization of the image is made. The threshold of the binary procedure is based on the isodata method [19] which is achieved in three steps: first, dividing the image into object and background by taking an initial threshold, then considering the pixels at or below the threshold and the pixels above. Finally, the averages of those two values are calculated and the threshold is incremented. The process is repeated until the threshold is larger than the composite average.

The last parameter to evaluate is the noise  $\epsilon_n$ . We can notice a very high-count value at  $C(x, y) < 1 \text{ rad/m}^2$  (Figure 1) corresponding to all the other pixel values of the image related to the numerical noise simulated and reported by a cyan pixel alert. We can also distinguish the contribution of  $\epsilon_n$  from  $\epsilon_a$  simply by visual interpretation: aliasing alerts should be on a local area of the image such as the edge of the simulated PMMA cylinder, where phase variations are not well described compared to noise alerts where those alerts contribution are more uniform on the image area. This implies that there are local intense blue alerts in the case of aliasing and uniform less intense cyan pixels alerts in the case of the presence of noise.

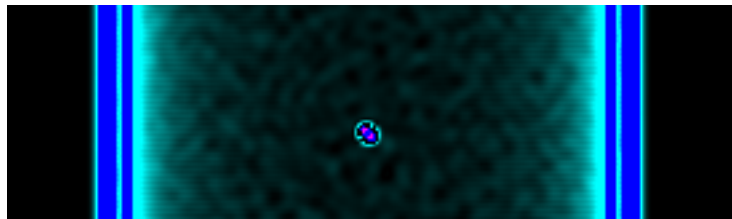


Fig. 2. Confidence map computed from the derivative closure map presented in Figure 1

Figure 2 present the computed confidence map with red pixel alerts in the center of the PMMA cylinder corresponding to a local extinction due to the defect simulated (see Figure 1). Blue pixels alerts on the edge of the cylinder are present due to the poor sampling on the edge of the cylinder. Cyan alerts are more distributed on the image with more intensity inside the sample. The confidence map presented on Figure 2 emphasizes the visual aid of this tool in detecting possible artifacts induced by the phase treatment. It will be used in the next section on real X-ray phase contrast image.

### 3. Experimental results

We will now focus on experimental results obtained from a canonical object, an optical fiber made of PMMA material with a diameter of  $500\ \mu\text{m}$ . Figure 3 presents the experimental arrangement. Multilateral shearing interferometry is used as differential phase contrast technique [16]. A micro-focus X-ray tube (Feinfocus FXE-160.51) measured spot size of  $5.5\ \mu\text{m}$  [20] with a solid transmitted Tungsten anode is used at tube intensity of  $60\ \mu\text{A}$  and tension of  $75\ \text{kV}$ . The detector is a Hamamatsu C12849-102U high resolution sensor made of a  $20\ \mu\text{m}$  layer of Gadox scintillator deposited on fiber plate coupled with a sCMOS sensor. The detector pixel size is  $6.5 \times 6.5\ \mu\text{m}^2$ . This imaging setup can achieve a spatial resolution limit of  $4.6\ \mu\text{m}$ , according to the Rayleigh criterion estimated with an image quality indicator (X-radia type X500-200-30) magnified by a factor of  $G = 19$  [21]. The following experimental images are the result of an average of 15 images with an exposure time of 20 seconds per image. The source-detector distance is  $d_{sd} = 57\ \text{cm}$  and the source-object and source-grating distances are, respectively  $d_{so} = 11\ \text{cm}$  and  $d_{sg} = 14\ \text{cm}$ , implying a magnification factor of roughly  $G = 5$  for the fiber and  $G = 4$  for the grating.

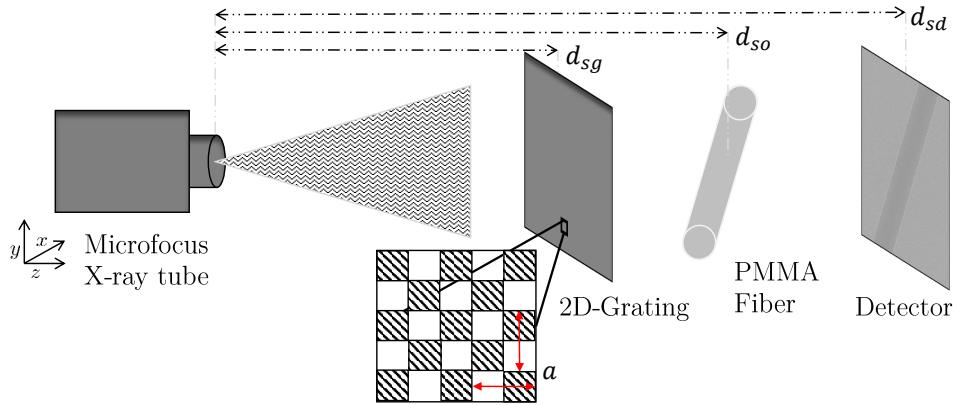


Fig. 3. Experimental arrangement with a polychromatic divergent microfocus X-ray source, a variation of the grating periodicity  $a = [24, 20, 16, 12]\ \mu\text{m}$  and a high-resolution detector.

Figure 4 presents the experimental results made with a single 2D-checkerboard phase grating (made by the Microworks company) of orthogonal periodicity of  $24\ \mu\text{m}$ . A  $[0-\pi]$  shifting at  $17.48\ \text{keV}$  is induced by Gold material of  $3.49 \pm 0.16\ \mu\text{m}$  thickness, deposited on a polymer substrate. At the top of the Figure 4, from left to right we present the raw image, the phase gradient and the phase image. The phase image is extracted by applying the Fourier derivative theorem [22] pre-treated by an anti-symmetric derivative integration proposed by P. Bon *et al* [23]. Multilateral shearing interferometry technique allows a direct measurement of phase gradient in multiple spatial directions. Therefore, we can use a derivative closure map (Eq. (1)) to get direct feedback of the measurement as presented in Figure 4 bottom left. This image highlights different areas, especially at the fiber edges and some pixels with extreme gray values. As described above, treatments on the phase derivative closure map are applied in order to get a confidence map. This confidence map is merged with the gradient and phase images as presented on Figure 4 bottom, middle and right. For a better visualization of the merged images, cyan alerts are not displayed. As we can see, local phase dislocations are present (orange arrows related to the yellow arrows on

the phase derivative closure map image), revealed with red alerts, as well as under sampling on the edges of the fiber corresponding to blue alerts. In particular, we can see that, some blue alerts are present inside the fiber, on the phase image merged with the confidence map (see red arrow).

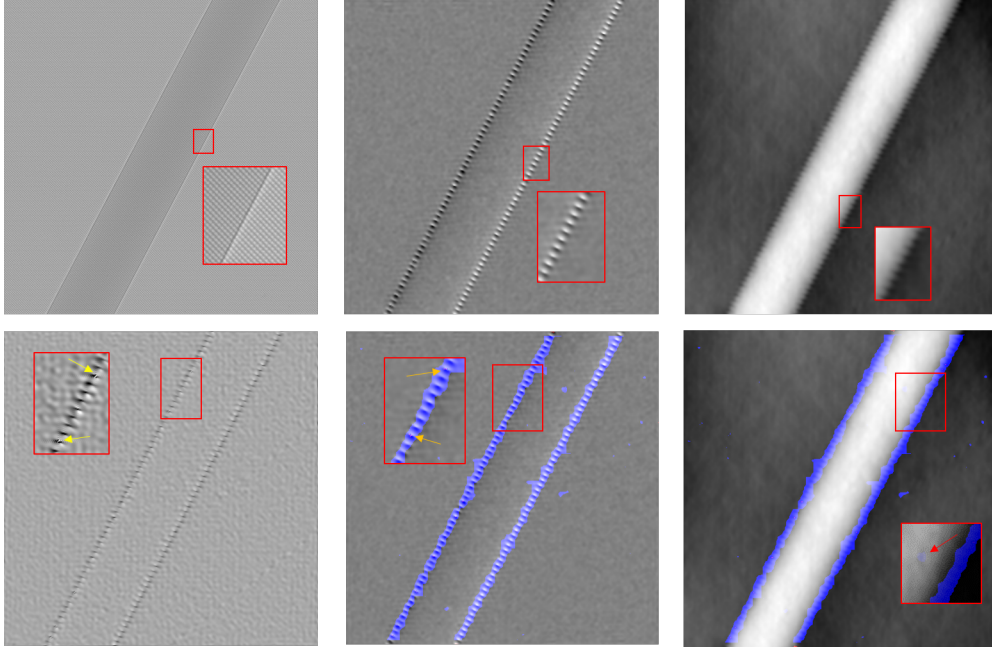


Fig. 4. Top row: raw image made with grating orthogonal periodicity of  $24\ \mu\text{m}$  (left); phase gradient (middle); phase image (right). Bottom row: phase derivative closure map (left); merge of the confidence map and the phase gradient (middle); merge of the confidence map and phase image (right).

To highlight the use of the confidence map, four acquisitions were made in the same experimental conditions with the same fiber position but for different grating periodicities (orthogonal direction), i.e.  $12\ \mu\text{m}$ ,  $16\ \mu\text{m}$ ,  $20\ \mu\text{m}$  and  $24\ \mu\text{m}$ . Figure 5 presents the phase image and the merge with the confidence map produced respectively with a grating of orthogonal periodicity of  $20\ \mu\text{m}$  (top row) and  $12\ \mu\text{m}$  (bottom row). The sample edge definition on the phase images improves with the diminution of the grating periodicity as confirm with the blue and red alert of the associate confidence maps. More generally, a clear improvement of the phase image is visible and is correlated to the sampling of the grating periodicity with a decreasing number of aliasing alerts (blue pixels). More precisely, the number of blue alerts drops from 6.15 % of the total pixel image to 1.83 % with the use of orthogonal grating periodicity of  $24\ \mu\text{m}$  and  $12\ \mu\text{m}$  respectively (3.12 % and 2.32 % for the grating periodicity of  $20\ \mu\text{m}$ ,  $16\ \mu\text{m}$ ). The number of phase dislocation alerts is also decreased for the  $24\ \mu\text{m}$ ,  $20\ \mu\text{m}$  and  $16\ \mu\text{m}$  with a significant increase for the  $12\ \mu\text{m}$  orthogonal grating periodicity (see the left histogram on Figure 6). The noise value related to the phase measurement (cyan alerts, not display on Figure 4 and 5) is quite stable for all grating configurations tested (see the right histogram on Figure 6).

#### 4. Discussion

All gradient based X-ray phase contrast techniques require a post treatment of the image acquisitions in order to extract the phase information. These treatments can cause artifacts and induce incorrect interpretations. The example of the canonical PMMA sample presented in

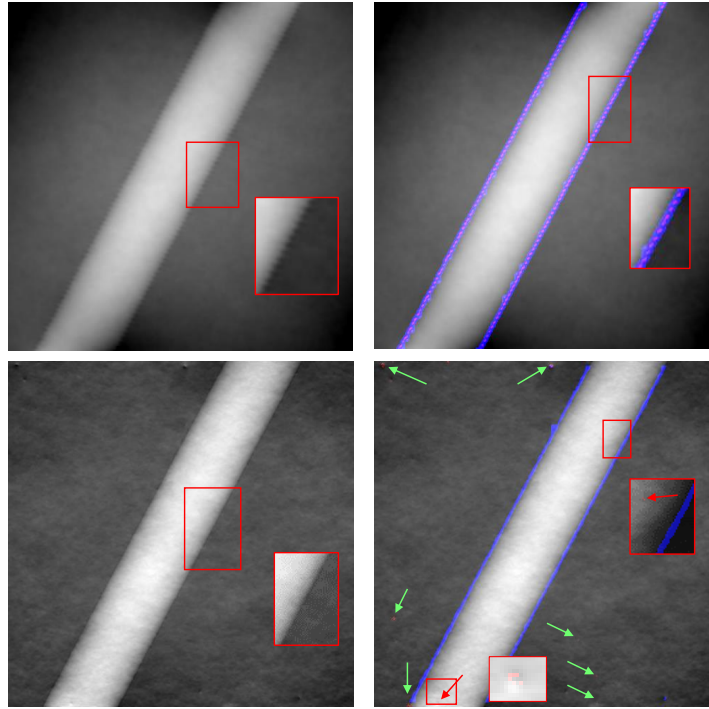


Fig. 5. Phase images (left) made with a grating orthogonal periodicity of 20  $\mu\text{m}$  (top row) and 12  $\mu\text{m}$  (bottom row) with the corresponding confidence map merging (right).

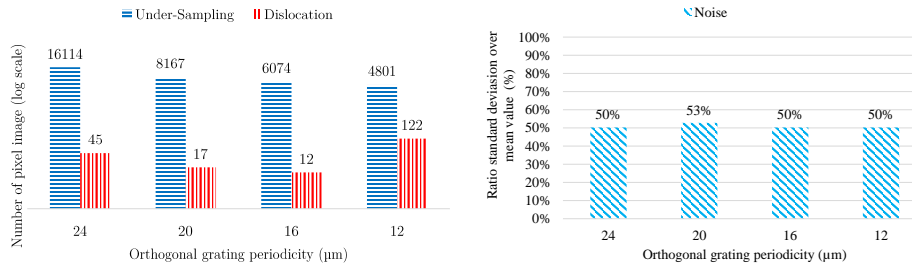


Fig. 6. Histogram of the evolution of the under-sampling and phase dislocation alerts as a function of the orthogonal grating periodicity (left). Histogram of the evolution of the noise alert calculation by taking the ratio standard deviation over the mean of the noise alert value, as in function of the orthogonal grating periodicity (right)

Figures 2 and 3, gives a first indication of what level of confidence we can have at the edge of the phase object. Indeed, in this area, a saw-tooth shape appears, leading to a confusing interpretation of the intrinsic shape of the sample for more complex geometries. The phase derivative closure map gives a first information but in order to connect the gray intensity value to physical information, the confidence map is built and displayed on the phase measurement images (see Figure 4 and 5).

As expected, there is a clear decrease in the phase dislocation and under-sampling alerts when the fringe sampling increases, except in the case of phase dislocation alerts related to the use of a

grating orthogonal periodicity of 12  $\mu\text{m}$ . This can be explained by the larger number of red pixel alters outside of the sample (see green arrows on Figure 5) compared to those inside the sample (see red arrow). This is most likely due to local grating flaws which can induce abrupt local phase variations leading to a red pixel alert made by the confidence map algorithm. So the confidence map can provide alerts not only relating to the quality of the image sample produce but also on the quality of the material used for the measurement (here a 2D-checkerboard grating). Finally, the stable value of the noise emphasize that  $\epsilon_n$  is not dependent on grating periodicity variations but more on the Fourier demodulation used to obtain the gradients and phase images.

The confidence map is really a qualification of the results given by the  $C(x, y)$  calculation, not linked to an *a priori* evaluation of the performance of the set-up, but directly evaluated from the data themselves. Therefore, an image interpreter can be directly alerted to the fact that the saw-tooth shape on the edges of the sample is truly an artifact. This is very interesting especially when the shape and texturing of an object of interest give important information as, for example, breast cancer diagnostics [24] where certain malignant tumors have edge texturing different from those that are benign. From the point of view of an experimenter, the confidence map is a very useful tool for improving the acquisition configuration. As we can see on the grating periodicity variation (Figure 5) if the goal is to make a measurement of the phase variation at the center of the PMMA fiber, edges are less important and a grating periodicity of 24  $\mu\text{m}$  can be considered. On the other hand, if the experimenter wants to optimize the edge PMMA fiber measurement, the best choice is a grating periodicity of 12  $\mu\text{m}$ . The confidence map is a means of attaining the best compromise in terms of acquisition parameter and image quality.

## 5. Conclusion

Our aim in this communication has been to present a tool we call the confidence map applicable to X-ray phase differential techniques. The confidence map provides a means of optimizing an experimental set-up, but is also an important tool for an end-user who must interpret the final image and make decisions based on it. As an optimization tool the confidence map can highlight the phase measurement sensitivity required and the possible flaws linked to the experimental set-up. As an aid for image interpretation, the confidence map has clear and simple color alerts, with a possible merging with the phase images produce.

This approach can be adapted to any type of X-ray differential phase contrast technique. It was applied here to a micro focus X-ray tube using multi-lateral shearing interferometry allowing a multiple direction phase derivatives evaluation from one measurement. For future work in phase contrast tomography, confidence maps can be used as prior input to minimize the artifact propagation in the iterative tomography process, such as SART or SIRT [25, 26].

**Disclosures.** The authors declare no conflicts of interest.

**Data availability.** The data presented in this study are available from the corresponding author on reasonable request.

## References

1. M. Endrizzi, "X-ray phase-contrast imaging," Nucl. instruments methods physics research section A: Accel. spectrometers, detectors associated equipment **878**, 88–98 (2018).
2. K. S. Morgan, D. M. Paganin, and K. K. Siu, "X-ray phase imaging with a paper analyzer," Appl. Phys. Lett. (2012).
3. S. Bérújon, E. Ziegler, R. Cerbino, and L. Peverini, "Two-dimensional x-ray beam phase sensing," Phys. Rev. Lett. (2012).
4. M. Stockmar, P. Cloetens, I. Zanette, B. Enders, M. Dierolf, F. Pfeiffer, and P. Thibault, "Near-field ptychography: phase retrieval for inline holography using a structured illumination," Sci. Rep. **3**, – (2013).
5. A. Momose, S. Kawamoto, I. Koyama, Y. Hamaishi, K. Takai, and Y. Suzuki, "Demonstration of x-ray talbot interferometry," Jpn. J. Appl. Phys. (2003).
6. T. Weitkamp, A. Diaz, C. David, F. Pfeiffer, M. Stampanoni, P. Cloetens, and E. Ziegler, "X-ray phase imaging with a grating interferometer," Opt. Express (2005).

7. F. Pfeiffer, T. Weitkamp, O. Bunk, and C. David, "Phase retrieval and differential phase-contrast imaging with low-brilliance x-ray sources," *Nat. Phys.* (2006).
8. K. S. Morgan, D. M. Paganin, and K. K. Siu, "Quantitative x-ray phase-contrast imaging using a single grating of comparable pitch to sample feature size," *Opt. Lett.* (2011).
9. H. H. Wen, E. E. Bennett, R. Kopace, A. F. Stein, and V. Pai, "Single-shot x-ray differential phase-contrast and diffraction imaging using two-dimensional transmission gratings," *Opt. Lett.* (2010).
10. H. Lim, Y. Park, H. Cho, U. Je, D. Hong, C. Park, T. Woo, M. Lee, J. Kim, N. Chung, J. Kim, and K. Jinguk, "Experimental setup and the system performance for single-grid-based phase-contrast x-ray imaging (pcxi) with a microfocus x-ray tube," *Opt. Commun.* (2015).
11. S. Tahir, S. Bashir, C. MacDonald, and J. C. Petrucci, "Mesh-based phase contrast fourier transform imaging," *Opt. Commun.* **389**, 103–109 (2017).
12. J. Rizzi, T. Weitkamp, N. Guérineau, M. Idir, P. Mercère, G. Druart, G. Vincent, P. da Silva, and J. Primot, "Quadriwave lateral shearing interferometry in an achromatic and continuously self-imaging regime for future x-ray phase imaging," *Opt. Lett.* (2011).
13. R. Jennison, "A phase sensitive interferometer technique for the measurement of the fourier transforms of spatial brightness distributions of small angular extent," *Mon. Notices Royal Astron. Soc.* (1958).
14. J. Rizzi, P. Mercère, M. Idir, P. D. Silva, G. Vincent, and J. Primot, "X-ray phase contrast imaging and noise evaluation using a single phase grating interferometer," *Optique Express* (2013).
15. D. L. Friedl, "Least-square fitting a wave-front distortion estimate to an array of phase-difference measurements," *J. Opt. Soc. Am. A* (1977).
16. J. Primot and N. Guérineau, "Extended hartmann test based on the pseudoguiding property of a hartmann mask completed by a phase chessboard," *Appl. Opt.* (2000).
17. J. N. Kapur, P. K. Sahoo, and A. K. Wong, "A new method for gray-level picture thresholding using the entropy of the histogram," *Comput. vision, graphics, image processing* **29**, 273–285 (1985).
18. A. G. Shanbhag, "Utilization of information measure as a means of image thresholding," *CVGIP: Graph. Model. Image Process.* **56**, 414–419 (1994).
19. T. Ridler, S. Calvard *et al.*, "Picture thresholding using an iterative selection method," *IEEE trans syst Man Cybern* **8**, 630–632 (1978).
20. NF - EN 12543-5, "Non-destructive testing. characteristics of focal spots in industrial x-ray systems for use in non-destructive testing. part 5 : measurement of the effective focal spot size of mini and micro focus x-ray tubes," *Tech. rep.*, AFNOR (1999).
21. P.-A. Douissard, A. Cecilia, X. Rochet, X. Chapel, T. Martin, T. van de Kamp, L. Helfen, T. Baumbach, L. Luquot, X. Xiao *et al.*, "A versatile indirect detector design for hard x-ray microimaging," *J. Instrumentation* **7**, P09016 (2012).
22. R. Bracewell, "The fourier transform and its applications," *McGraw-Hill Electr. Electron. Eng. Ser.* **5** (1965).
23. P. Bon, S. Monneret, and B. Wattelier, "Noniterative boundary-artifact-free wavefront reconstruction from its derivatives," *Appl. Opt.* (2012).
24. S. Ray, N. D. Prionas, K. K. Lindfors, and J. M. Boone, "Analysis of breast ct lesions using computer-aided diagnosis: an application of neural networks on extracted morphologic and texture features," in *Medical Imaging 2012: Computer-Aided Diagnosis*, vol. 8315 (International Society for Optics and Photonics, 2012), p. 83152E.
25. A. H. Andersen and A. C. Kak, "Simultaneous algebraic reconstruction technique (sart): a superior implementation of the art algorithm," *Ultrason. imaging* **6**, 81–94 (1984).
26. P. Gilbert, "Iterative methods for the three-dimensional reconstruction of an object from projections," *J. theoretical biology* **36**, 105–117 (1972).